Anomalous thermophysical properties and electride transition in fcc potassium

Anomalous thermophysical properties and electride transition in fcc potassium

Long Zhao [1], Hongxiang Zong [1, 2], Xiangdong Ding [1], Jun Sun [1], Graeme J. Ackland [2]

[1]*State Key Laboratory for Mechanical Behavior of Materials, Xi'an Jiaotong University, Xi'an, Shanxi 710049, China*

[2] *Centre for Science at Extreme Conditions (CSEC), School of Physics and Astronomy, University of Edinburgh, Edinburgh EH9 3FD, UK*

**To whom correspondence should be addressed. E-mail: zonghust@mail.xjtu.edu.cn, dingxd@mail.xjtu.edu.cn*

Abstract

Alkali metals undergo an electride transition with excess electrons localized into interstices and acting as anionic interstitial quasi-atoms (ISQs). Less is known about the role of electride transition in changing their thermophysical properties. Here, taking potassium as an example, we investigated the thermodynamic and dynamic properties in the fcc phase region where an electride transition occurs when increasing pressure. With the help of machine-learning enhanced molecular dynamic simulations and DFT calculations, we show property anomalies over a wide pressure range of 10 - 20 GPa but no accompanying structural transformations. Furthermore, we find that these anomalies in solid potassium are stronger at lower temperatures due to the more electron-localized nature of ISQs. Our findings unveil the rich phenomena in electrides, and could deepen our understanding on electride phase transition.

I. INTRODUCTION

Alkali metals are often considered to be “simple” metals as their electronic properties can be well described by nearly free-electron models at ambient conditions [1, 2]. Under pressure, however, there is growing evidence that alkali metals exhibit many striking phenomena, such as anomalous melting behavior [3-5], the emergence of low-symmetry complex structures [6], and so on [7]. One of the most fascinating ones is the high-pressure electride (HPE) that was first predicted by theoretical models [8] and then has been confirmed by diamond-anvil cell experiments recently [9]. HEPs differ from traditional electrides in that the thermodynamic reason to form ISQs is primarily volume reduction, rather than ionicity. HPEs are often metallic, and there is no evidence for paramagnetism [10].

HPEs, in which electrons occupy interstitial regions in crystal and behave as anions, often exhibit unique electromagnetic properties. A pioneering study on Na shows that a pristine metal could become an insulator in HPE state when suffering from a pressure high than 200 GPa [9, 11, 12]. Following experimental and theoretical works also demonstrated that Li transforms into a semiconductor HPE with a gap of 0.3eV at 80GPa [13-16]. Simultaneously, the absorption spectrum of Na-HPE is strongly anisotropic, i.e., sodium becomes optically transparent in one direction but reflective in the other ones [11]. Besides, the reflectivity of both solid and liquid alkali metals (mainly lithium [17] and potassium [18]) shows a slight dip across the electride transition region. Furthermore, it is found that the electron and phonon interaction in HPE state can give rise to an anomalous LA-TA splitting in the phonon

dispersion [19]. This indicates that an electride transition under high pressure can strongly change the motion of ion cores in solid-phase state, thus the dynamic properties of materials. However, to the best of our knowledge, there are few studies on the thermodynamic or dynamic properties of materials considering the effect of electride transition. Although our recent work on potassium liquid has shown remarkable thermodynamic or dynamic anomalies induced by the atom-to-electride transition, which is accompanied by shape change of local structures [18], it is unclear whether these anomalous companying the atom-to-electride transition still exists in solid-state phase without structural transformation.

Herein, we utilized a machine-learning enhanced molecular dynamic simulation and DFT calculation to explore the thermodynamic and dynamic properties of fcc potassium, which is expected to undergo an atom-to-electride transition under pressure. We note that the evolution of thermodynamic and vibrational properties shows anomalies over a wide pressure range of 10 - 20 GPa. These abnormalities are derived from the electride transition instead of structural transformation. Furthermore, we find that these anomalies in solid are stronger at lower temperatures due to the more electron-localized nature of ISQs. To this end, we modified the phase diagram of solid potassium in fcc stable region.

II. METHODS

A domain knowledge-based machine learning approach is adopted to match the true potential energy surface of potassium [18, 20, 21]. The first principle calculations

of potassium can well capture the phase stability and physical properties from experimental observation, e.g., more accurate melting points can be achieved via AIMD simulation of the liquid and solid coexistence [22] (see Fig. 2). Therefore, the machine learning interatomic potential (MLIP) is directly learned from an accurate reference database of first principles calculations [25] using the Vienna ab initio simulation package (VASP) [26]. The full database is accumulated from the AIMD simulation of bcc, fcc, KIIIa, and corresponding liquid structures at different temperatures and pressures. The training dataset and testing dataset are randomly selected from the database with a proportion of 9:1. Then, we adopted a linear regression algorithm, in which the coefficients are fitted by using the kernel ridge regression method [27]. A more detailed description of this machine learning potential can be found in Ref. [21]. In addition, the performance of MLIP has been evaluated by comparing machine learning prediction with the corresponding DFT calculation. As shown in Fig. 1, the low mean absolute error (MAE) for both potential energy (~ 1.3 meV/atom) and atomic force (~ 0.018 eV/Å) suggests a high fidelity of our machine learning potential. This machine learning potential can well reproduce the phase diagram of potassium (see Fig. 2) [18, 21], except a slightly vertical shift of melting curve comparing experimental data. We believe this discrepancy results from the size effect, i.e., the limited size of samples in simulations without considering crystal defects (such as dislocations, grain boundaries, and so on), which can act as heterogeneous nucleation centers of the liquid phase and lower the melting temperatures [28]. In addition, it has successfully been applied to capture the

liquid-liquid phase transition (LLPT) induced by electride transitions [18]. Therefore, it allows us to utilize this MLIP to explore the evolution of thermodynamic and dynamic properties in solid potassium across electride phase transition.

Classic molecular dynamic (MD) simulations with a machine-learning interatomic potential (hereafter refer to MLMD) were then performed to study the dynamics of fcc potassium with a time step of 1fs, and periodic boundary conditions were applied along all three dimensions. MD simulations are run at a fixed density (NVT) with a Nose-Hoover thermostat [29]. All MD simulations were carried out using the LAMMPS package [30] and the atomic configurations were visualized with the VESTA [31]. Typical samples of fcc potassium containing up to 4000 atoms were used to study the corresponding thermophysical properties of solid (such as isothermal bulk modulus B_T, heat capacity C_p, thermal expansion α ,and compressibility β) at selected pressures and temperatures. In addition, to eliminate the possible size effect, we also perform MD simulation of larger samples with 13500 atoms, which show a similar tendency in the pressure dependence of physical properties involved (see Fig. 1).

DFT calculations were performed using the VASP [26]. The generalized gradient approximation (GGA) was used in the scheme of Perdew-Burke-Ernzerhof (PBE) to describe the exchange-correlation functional [32]. AIMD simulations were utilized in 3×3×3 supercells (with 128 atoms for potassium) with a plan-wave cutoff energy of 450 eV and a denser k-point mesh of 3×3×3. A Nose-Hoover thermostat was used to perform the NVT simulations. For each AIMD simulation, the structure was

generated at the appropriate density and held at constant temperatures for 6000 steps with time step of 3 fs. The initial 3 ps were used for the thermalization and the final 5000 steps of each trajectory were used to extract the statistical quantities. The vibrational density of state (VDOS) at 0 K were calculated using the density-functional perturbation theory method as implemented in the PHONOPY package [33] and finite-temperature renormalized VDOS were performed using phonon mode decomposition and AIMD's projection technique implemented in DYNAPHOPY [34]. In addition, analyzing the non-nuclear charge was performed using the Bader partitioning scheme [35] for the charge density. At each pressure, 20 snapshots were averaged for charge density and electron localization function (ELF) [36] calculations.

III. RESULTS

A. Atom-to-electride transition

The proposed atom-to electride transition in potassium is first confirmed by studying the electronic properties at selected temperatures (50 and 150 K) within the fcc stable region (10 - 20 GPa). Curves of non-nuclear charge maxima and average value counted by Bader analysis [35] are shown in Fig. 3(a). At 50 K, both the curves of pressure-dependent maximum and averaged non-nuclear charge is gradually increased from ~ 0.06 (at 11 GPa) to ~ 0.12 (at 14 GPa), then start to saturate above 14 GPa. This indicates that fcc potassium undergoes a transition from atomic-like state to electride-like state. Although the non-nuclear charge at both 50 K and 150 K

shows a similar atom-to electride transition, their pressure dependence is different, i.e, the non-nuclear charge at 50 K shows a sharper change than that of 150 K when across the pressure of ~ 11 - 14 GPa, suggesting a temperature effect in fcc potassium. In addition, the average (~ 0.5) and maximum (~ 0.6) non-nuclear electron of KIIIa at 22 GPa and 0 K is calculated (see the black and red dash line in Fig. 3(a)), we note that the full electride nature of KIIIa is of higher-intensity than fcc phase (around 1/5 of KIIIa) which indicates the interstitials of fcc structure are partially filled by the electrons. We plot the change of the electron localization function (ELF) along [100] direction in Fig. 3(b). We note that ELF at interstitial sites is ~ 0.73 (larger than 0.5), and gradually increases with the increases of pressure (as pointed out by the black arrows in Fig. 3(b)), consistent with the stronger localized nature of electrons at the interstitial sites upon electride transition. Figures 3(c)-(e) show the spatial distribution of ELFs at 50K, which confirms the strong localization of electrons at octahedral interstitial sites. fcc has one such octahedral site per atomic site. The non-nuclear ELF maxima (non-circular red blobs) become more pronounced as we increase the pressure from 9 GPa to 19 GPa, consistent with our Bader analysis in Fig. 3(a). Fig. 3(f) relates the Bader and ELF analyses, confirming that the non-nuclear Bader value is associated with the region of localized electrons, i.e., high values of ELF.

Subsequently, we investigated the corresponding structure factor $S(q)$ as a function of pressure in Fig. 4. Here, $S(q)$ is calculated by a Fourier transform of the corresponding radial distribution functions (RDFs), and can be directly measured by diffraction experiments. In Fig. 4(a), $S(q)$ for different pressure cases share a similar

feature except a slight shift of the peaks, which reflects the structural evolution with volume (density) variance under pressure. To quantify this, we calculated the corresponding Q_1/Q_{10} (where Q_1 is the position of the first peak in $S(q)$ at selected pressures while Q_{10} is the reference position of the first peak at 10.9 GPa) in the insert of Fig. 4(a), whose pressure dependence shows a continuous nature, indicating the absence of accompanying significantly structural change in this pressure region. Furthermore, the evolution of normalized structure factor by Q_1 at selected pressures for both 50 K and 250 K are shown in Figs. 4(c)-(d) (Q_1 is the position of the first peak of structure factor functions). Interestingly, all the peaks at different pressures almost exactly coincide, lending credence to the occurrence of pressure-induced isostructure transition. What's more, different from the electronic properties shown in Fig. 3, the structural motif shows no temperature dependence, as demonstrated by comparing $S(q)$ of 50 K and 250 K in Fig. 4. Therefore, fcc potassium in this pressure region can serve as an ideal test-bed for us to focus on the effect of atom-like to electride-like transition on the thermodynamic or dynamic properties of solid phases under high pressure.

B. Thermodynamic properties

Figure 5 shows the thermal expansivity α, compressibility β, heat capacity C_p and density of state (EOS) as a function of pressure. The thermal expansion coefficient α wase first calculated in Fig. 5(a), and systematically observing in different temperature data demonstrates an anomalous behavior. The thermal

expansion curves have local maxima and minima in this pressure region with a strong dip between 9 and 12 GPa. The dip is gradually weakened as the temperature rises, which is consistent with the electrical resistance evolution upon heating at 13 GPa [24]. The same anomaly is true for the compressibility β and the heat capacity C_p, i.e., fcc potassium is more compressible but has lower heat capacity in the pressure crossover region at low temperatures (below 300 K), see Fig. 5(b) and 5(c). It is important to point out that these anomalies gradually disappeared at high temperatures (above 350 K but below melting point). We note that the region of all these thermodynamic anomalies is almost consistent with the atom-to-electride transition regime in Fig. 3(a). In addition, to explore the effect of electride transition, we checked the EOS by calculating the corresponding pressure dependence of density. However, we see no measurable density discontinuity along the EOS curves (see Fig. 5(d)). It suggests that this is a continuous phase transition, similar to what we have found in the high-temperature region with a liquid-liquid phase transition [18].

To check the reliability of MLMD simulation result, the MLMD and AIMD data of isothermal bulk modulus, related to density by $B_T = \rho(\partial P / \partial \rho)_T$, including 50, 150, and 350K, are compared in Fig. 6. Both data show a similar tendency in the pressure dependence of B_T, and a clear bump occurs at around 16 GPa, which indicates the remarkable change of slope in B_T curve. This is concordant with the other thermodynamic anomalies (α, β, and C_p) in Fig. 5. Also, a similar B_T anomaly has also been observed in dense potassium liquid [18] and rubidium liquid [37]. This consistency indicates the reliability of our MLMD simulation results, i.e, the

anomalies of thermodynamic properties indeed exist in fcc potassium, consistent with the presence of an electride transition in the region of 10 - 20 GPa. Besides, it is important to note that the temperature dependence of B_T anomaly is slightly different in MLMD and AIMD simulations. This is demonstrated by that the B_T anomaly is weakened with temperature in MLMD while independent of temperature in AIMD (see the inset of Fig. 6). We believe this difference is a result of the size effect, i.e., a small sample size is adapted in AIMD simulations, which has been revealed by our previous work on liquid potassium [18]. Also, the slight differences of B_T between MLIP and AIMD at low pressures, which may result from the size effect or limited performance of machine learning potential in describing the high-order elastic constant, do not significantly reduce the reliability of our main findings.

C. Dynamic properties

Direct information on the dynamics of a system can be captured by the phonon band structures and vibrational density states (VDOS) obtaining by lattice dynamic calculation [38]. Therefore, the phonon dispersions and the VDOSs of fcc potassium across the electride transition are calculated in Fig. 7. Fig. 7(a) shows the phonon dispersions of fcc potassium from 13 to 17 GPa at 0 K which is consistent with the clarifications of experiments and theoretical calculations that the fcc potassium is a stable phase in the wide of range pressures (~ 11.6 – ~ 20 GPa) [39, 40]. Fig. 7(b) shows the effect of pressure on the VDOSs of fcc potassium from DFT calculation at 0 K. Profiles of VDOSs with two main peaks show typical fcc structural features with

a shoulder in the first peak (located around ~ 1.5 THz) [41], and the shoulder gradually shift to high frequency besides a sharply change between 14 GPa and 16 GPa. This agrees well with the atom-to-electride transition. Furthermore, Fig. 7(c) shows the frequency of the shoulder of the first main peak as a function of pressure. We find an anomalous evolution of the frequency, i.e., display a clear bump at ~ 16 GPa. This manner is similar to the abnormality showed in isothermal bulk modulus (see Fig. 6). The phonon dispersion curves of different temperatures at 14 GPa are captured by the normal-mode-decomposition technique [34]. This method incorporates the phonon-electron coupling effect related to the electride state, equivalent to the non-analytic terms in Zhang's model [19], which show imaginary frequencies due to the contribution of electride, as shown in Fig. 7(d). We find that he density of imaginary frequency is gradually enhanced when the temperature decreases. It is consistence with Zhang's model, which suggests that the imaginary frequency in electride materials is strongly correlated with the effective mass of ISQs [19].

The Debye-Waller factor (B_k), which characterizes the effect of lattice vibrations [42], is related to $<\boldsymbol{r}^2>$ or the mean square displacement, and $B_k = \frac{8\pi^2}{3} < r^2 >$. Figure 8 shows the B_k of fcc potassium as a function of pressure along different isotherms ranging from 50 to 350 K. The B_k curves at low temperatures show an anomaly with a local maximum at around 14 GPa, which suggests that the amplitude of lattice vibrations is gradually enhanced across the atom-to-electride transition, similar to the effect of temperature [43]. The maximum points of B_k at various temperatures can be estimated from the cubic spline curve based on the MLMD data, as shown in the inset

of Fig. 8. Interestingly, the anomaly in B_k of fcc potassium as a function of pressure gradually decays when the temperature rises, and almost disappeared at 350 K. In this aspect, it agrees well with the temperature-dependent thermodynamic properties of solid potassium in Figs. 4(a)-(c).

IV. DISCUSSION

The main focus of our study is the anomalous behavior of a range of thermodynamic properties – specifically maxima and minima along isotherms which trace Widom lines in the PT phase diagram. These thermodynamic anomalies can be understood using a two-state Bragg-Williams-type (BW) model to describe the electride transition under compression, which enables us to further understand the nature of the electride state. The BW model is a mean-field approximation to Ising model [44], and here the spins are mapped into the "electride" or "electron" states, and the field is mapped to the enthalpy difference between the two states. In this scenario, the excess Gibbs Free Energy due to the electride transition is

$$G_{ET}(x) = x(\Delta U_e - PV_e - TS_e) + RT\left[x\ln x + (1-x)\ln(1-x)\right] + Jx(1-x) \quad (1)$$

Where x is the electride fraction, ΔU_e, ΔS_e and ΔV_e are the difference in the internal energy, entropy and volume between the normal and electride states, while J is a local coupling between electride and free electrons. These terms give immediate insight into the differences between free-electron and electride behavior. If J is repulsive, BW exhibits a solid-solid critical point at which all the thermodynamics anomalies converge; in potassium, we see no evidence of this, so we can assume that J is

attractive. The electride is the high-pressure phase, so ΔV_e must be positive. The free electron state is stable at low P, T so ΔU_e must also be positive. Temperature dependence comes from both the $T\Delta S_e$ term and the entropy of mixing.

The physical observables in BW including thermal expansivity, compressibility, and heat capacity can be calculated [45] as second derivatives of Min_x $G(P, T)$ and are illustrated in Fig. 9. The BW model well captures the temperature dependence of these anomalies: C_p has two maxima and a minimum; β has a single maximum; α has a minimum and a maximum. Inspired by water [46, 47], the maximum of compressibility (β) and the minimum of heat capacity (C_p) corresponds to a maximum thermal fluctuation when the population of electride and free-electron state is equal (see Fig. 9(d)). Furthermore, the abnormalities become smaller while the temperature increases. All these features are consistent with our simulation results, which include both the excess free energy from the electride transition and the 'normal' free energy from all other contributions, which we expect to be smoothly varying.

A particular feature of the BW model and the MLMD is the existence of a minimum in the heat capacity. In potassium, this moves to lower pressure as the temperature increases. The C_p minimum occurs when the crossover is primarily pressure-driven and occurs where the two states have equal enthalpy. In fact, the BW contribution to the heat capacity comprises two broad maxima, but it is small compared with phonon contributions and so the minimum between these broad maxima is the more easily-seen feature. The negative slope shows that ΔS_e is positive.

What's more, the electronic properties at various temperatures are calculated to understand the origin of the aforementioned temperature effect. Fig. 10(a) shows the temperature dependence of non-nuclear charge maxima and average value at 14 GPa. We find that both the maximum and averaged non-nuclear charge increase continuously with temperature before the melting point (T_m), and then soars into a high value after melting. It suggests a stronger electride nature of liquid phase, consistent with our previous work [18]. The corresponding ELF topology at selected temperatures below T_m is shown in Figs. 10(b)-(e). Noticeably, the non-nuclear ELF is more diffuse and spatially homogeneous at high temperatures (see Figs. 10(d)-(e)). This is the origin of the weaken imaginary of phonon dispersions as the temperature increases (see Fig. 7(d)), and it is quite different from the low temperature cases where the non-nuclear charge are more localized in the center of the interstitial lattice sites (see Figs. 10(b)-(c) and the 50 K curve at Fig. 7 (d)), and behaves more like anions. The enhanced electron localization of HPE at low temperature may result in a stronger coupling of lattice vibrations between potassium ion cores and these ISQs [19], which is a response to the anomalies in fcc potassium under pressure. In contrast, the lattice fluctuation that is intensified at high temperatures can distort local structures randomly, thus missing the localization characteristics of ISQs. In this scenario, such delocalized nature may completely disappear when approaching the melting point, leading to the absence of thermophysical property abnormalities. We speculate that there may exist a high order critical point at the crossing of the static

and dynamic Schottky lines [47], which is very close to the bcc-fcc-liquid triple point, as shown in Fig. 2.

V. CONCLUSION

In summary, we have investigated the thermophysical properties across the atom-to-electride transition in fcc potassium utilizing large-scale molecular dynamics simulations and ab into calculations. We find that pure atom-to-electride transition in solid phase without global structural phase change can still lead to thermodynamic and dynamic properties anomalies under high pressure. It is due to the coupling of local structural dynamics with emerging interstitial quasi-atoms upon compression. Besides, the dependence of HPE on temperature gives rise to a weakening anomaly of thermophysical properties at high temperatures. We suggest that the effect of atom-to-electride transition on the thermophysical properties cannot be underestimated in alkali metals and other materials that undergo electride transition under high pressure.

ACKNOWLEDGMENTS

This work was supported by the National Natural Science Foundation of China (51320105014, 51871177 and 51931004) and the 111 project 2.0 (BP2018008), the ERC grant “Hecate" and the China Postdoctoral Science Foundation (2020M673385).

[1] E. Wigner and F. Seitz, On the constitution of metallic sodium, Phys. Rev. **43**, 0804 (1933).

[2] F. S. Ham, Energy Bands of Alkali Metals .1. Calculated Bands, Phys. Rev. **128**, 82 (1962).

[3] E. Gregoryanz, L. F. Lundegaard, M. I. McMahon, C. Guillaume, R. J. Nelmes and M. Mezouar, Structural diversity of sodium, Science **320**, 1054 (2008).

[4] C. L. Guillaume, E. Gregoryanz, O. Degtyareva, M. I. McMahon, M. Hanfland, S. Evans, M. Guthrie, S. V. Sinogeikin and H. K. Mao, Cold melting and solid structures of dense lithium, Nat. Phys. **7**, 211 (2011).

[5] R. Boehler and C. S. Zha, Systematics in the Melting Behavior of the Alkali-Metals from Dac Measurements, Physica B & C **139**, 233 (1986).

[6] M. I. McMahon and R. J. Nelmes, High-pressure structures and phase transformations in elemental metals, Chem. Soc. Rev. **35**, 943 (2006).

[7] S. Falconi, M. I. McMahon, L. F. Lundegaard, C. Hejny, R. J. Nelmes and M. Hanfland, X-ray diffraction study of diffuse scattering in incommensurate rubidium-IV, Phys. Rev. B **73**, (2006).

[8] B. Rousseau and N. W. Ashcroft, Interstitial electronic localization, Phys. Rev. Lett. **101**, 046407 (2008).

[9] Y. M. Ma, M. Eremets, A. R. Oganov, Y. Xie, I. Trojan, S. Medvedev, A. O. Lyakhov, M. Valle and V. Prakapenka, Transparent dense sodium, Nature **458**, 182 (2009).

[10] J. L. Dye, Electrons as anions, Science **301**, 607 (2003).

[11] M. Gatti, I. V. Tokatly and A. Rubio, Sodium: A Charge-Transfer Insulator at High Pressures, Phys. Rev. Lett. **104**, (2010).

[12] M. Marques, M. Santoro, C. L. Guillaume, F. A. Gorelli, J. Contreras-Garcia, R. T. Howie, A. F. Goncharov and E. Gregoryanz, Optical and electronic properties of dense sodium, Phys. Rev. B **83**, 184106 (2011).

[13] T. Matsuoka and K. Shimizu, Direct observation of a pressure-induced metal-to-semiconductor transition in lithium, Nature **458**, 186 (2009).

[14] C. J. Pickard and R. J. Needs, Dense Low-Coordination Phases of Lithium, Phys. Rev. Lett. **102**, 146401 (2009).

[15] M. Marques, M. I. McMahon, E. Gregoryanz, M. Hanfland, C. L. Guillaume, C. J. Pickard, G. J. Ackland and R. J. Nelmes, Crystal Structures of Dense Lithium: A Metal-Semiconductor-Metal Transition, Phys. Rev. Lett. **106**, 095502 (2011).

[16] G. A. Adebayo, Ab initio calculations of optical properties of Li and K at high pressures, J. Phys. Chem. Solids **74**, 1221 (2013).

[17] Z. Yu, H. Y. Geng, Y. Sun and Y. Chen, Optical properties of dense lithium in electride phases by first-principles calculations, Sci. Rep. **8**, 3868 (2018).

[18] H. X. Zong, V. N. Robinson, A. Hermann, L. Zhao, S. Scandolo, X. D. Ding and G. J. Ackland, Free electron to electride transition in dense liquid potassium, Nat. Phys. **17**, 955 (2021).

[19] L. L. Zhang, H. Y. Geng and Q. Wu, Prediction of anomalous LA-TA splitting in electrides, Matter Radiat. at Extremes **6**, 038403 (2021).

[20] V. N. Robinson, H. X. Zong, G. J. Ackland, G. Woolman and A. Hermann, On

the chain-melted phase of matter, Proc. Natl. Acad. Sci. U.S.A. **116**, 10297 (2019).

[21] L. Zhao, H. X. Zong, X. D. Ding, J. Sun and G. J. Ackland, Commensurate-incommensurate phase transition of dense potassium simulated by machine-learned interatomic potential, Phys. Rev. B **100**, 220101 (2019).

[22] G. Boucher, First-principles study of the phase diagram of Potassium, Ph. D. thesis, University College London, 2019.

[23] E. E. McBride, K. A. Munro, G. W. Stinton, R. J. Husband, R. Briggs, H. P. Liermann and M. I. McMahon, One-dimensional chain melting in incommensurate potassium, Phys. Rev. B **91**, 144111 (2015).

[24] M. Sakata, Y. Nakamoto, T. Matsuoka, Y. Ohishi and K. Shimizu, Structural phase transition of potassium under high-pressure and low-temperature condition, J. Phys. Conf. Ser. **950**, 042020 (2017).

[25] G. Kresse and J. Furthmuller, Efficiency of ab-initio total energy calculations for metals and semiconductors using a plane-wave basis set, Comp. Mater. Sci. **6**, 15 (1996).

[26] G. Kresse and J. Furthmuller, Efficient iterative schemes for ab initio total-energy calculations using a plane-wave basis set, Phys. Rev. B **54**, 11169 (1996).

[27] B. Schölkopf and A. J. Smola, Learning with Kernels (MIT Press, Cambridge, 2002).

[28] A. Samanta, M. E. Tuckerman, T. Q. Yu and W. N. E, Microscopic mechanisms

of equilibrium melting of a solid, Science **346**, 729 (2014).

[29] S. Nose, A Unified Formulation of the Constant Temperature Molecular-Dynamics Methods, J. Chem. Phys. **81**, 511 (1984).

[30] S. Plimpton, Fast Parallel Algorithms for Short-Range Molecular-Dynamics, J. Comput. Phys. **117**, 1 (1995).

[31] K. Momma and F. Izumi, VESTA 3 for three-dimensional visualization of crystal, volumetric and morphology data, J. Appl. Crystallogr. **44**, 1272 (2011).

[32] J. P. Perdew, J. A. Chevary, S. H. Vosko, K. A. Jackson, M. R. Pederson, D. J. Singh and C. Fiolhais, Atoms, Molecules, Solids, and Surfaces - Applications of the Generalized Gradient Approximation for Exchange and Correlation, Phys. Rev. B **46**, 6671 (1992).

[33] A. Togo and I. Tanaka, First principles phonon calculations in materials science, Scripta Mater. **108**, 1 (2015).

[34] A. Carreras, A. Togo and I. Tanaka, DynaPhoPy: A code for extracting phonon quasiparticles from molecular dynamics simulations, Comput. Phys. Commun. **221**, 221 (2017).

[35] G. Henkelman, A. Arnaldsson and H. Jonsson, A fast and robust algorithm for Bader decomposition of charge density, Comp. Mater. Sci. **36**, 354 (2006).

[36] A. D. Becke and K. E. Edgecombe, A Simple Measure of Electron Localization in Atomic and Molecular-Systems, J. Chem. Phys. **92**, 5397 (1990).

[37] S. Ayrinhac, V. N. Robinson, F. Decremps, M. Gauthier, D. Antonangeli, S. Scandolo and M. Morand, High-pressure transformations in liquid rubidium,

Phys. Rev. Mater. **4**, (2020).

[38] D. Alfe, PHON: A program to calculate phonons using the small displacement method, Comput. Phys. Commun. **180**, 2622 (2009).

[39] G. Woolman, V. N. Robinson, M. Marques, I. Loa, G. J. Ackland and A. Hermann, Structural and electronic properties of the alkali metal incommensurate phases, Phys. Rev. Mater. **2**, 053604 (2018).

[40] O. Narygina, E. E. McBride, G. W. Stinton and M. I. McMahon, Melting curve of potassium to 22 GPa, Phys. Rev. B **84**, (2011).

[41] D. Srivastava, U. V. Waghmare and S. K. Sarkar, Evidence of scaling in the high pressure phonon dispersion relations of some elemental solids, J. Chem. Phys. **141**, 044714 (2014).

[42] S. Caravati, M. Bernasconi, T. D. Kuhne, M. Krack and M. Parrinello, First-principles study of crystalline and amorphous Ge2Sb2Te5 and the effects of stoichiometric defects, J Phys-Condens Mat **21**, (2009).

[43] C. M. Roland and K. L. Ngai, The anomalous Debye-Waller factor and the fragility of glasses, J. Chem. Phys. **104**, 2967 (1996).

[44] W. L. Bragg and E. J. Williams, The effect of thermal agitation on atomic arrangement in alloys, Proc. Roy. Soc. London, Ser.A. **151**, 699 (1934).

[45] G J. Ackland, H Zong, V Naden Robinson, S Scandolo, and A Hermann Two state model for critical points and the negative slope of the melting-curve Preprint: https://arxiv.org/abs/2103.07284.

[46] A. Nilsson and L. G. M. Pettersson, The structural origin of anomalous properties

of liquid water, Nat. Commun. **6**, 8998 (2015).

[47] R. Shi and H. Tanaka, The anomalies and criticality of liquid water, Proc. Natl. Acad. Sci. U.S.A. **117**, 26591 (2020).

Figure Captions

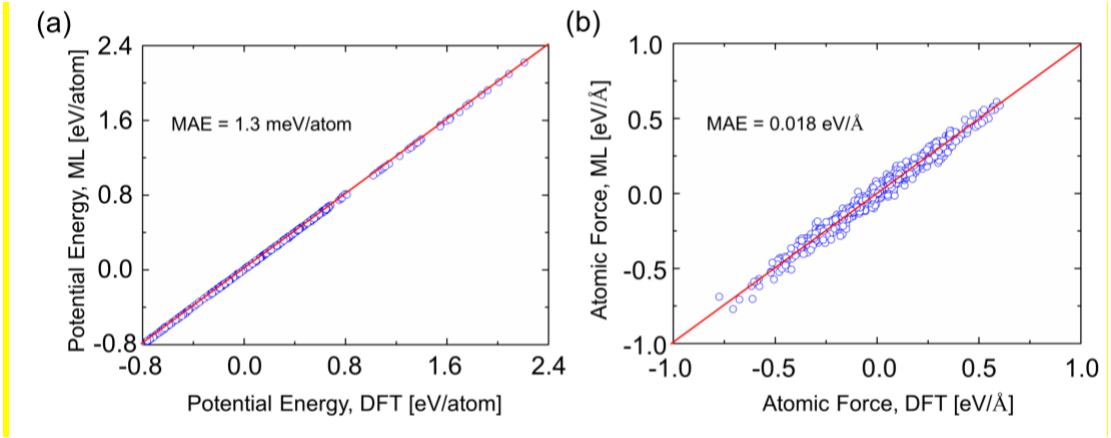

FIG. 1. Performance of our ML potential compared with the DFT references. (a) Per-atom potential energy and (b) Atomic force for configurations. A perfect correlation with the DFT values is shown by the red lines. MAE is the mean absolute error.

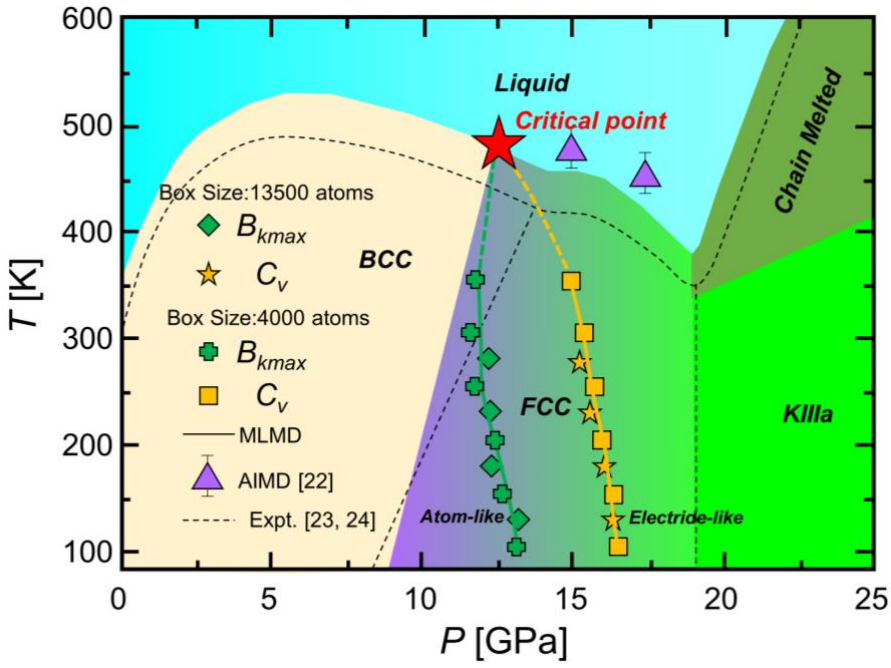

FIG. 2. Phase diagram of potassium as a function of temperature and pressure. The colors present the stability region of different phases. Dash lines are experimental phase boundaries (solid-solid, solid-chain melt, and solid-liquid) take from ref. [23, 24]. The purple triangles are the melting points detected by AIMD simulations with the solid-liquid coexistence method [22]. Green crossheads (rhombuses) and orange squares (pentagrams) show the maxima of the Debye-Waller factor ($B_k(P)$) and the minima of heat capacity C_V (P) curves at different temperatures, respectively. The critical point here is defined by the crossing of the green and orange lines.

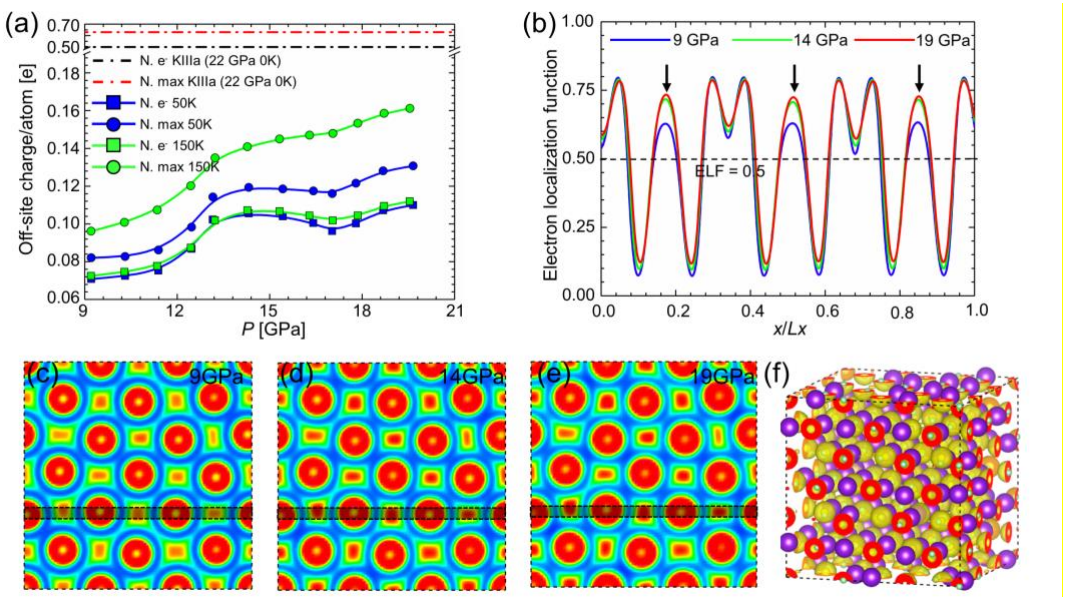

FIG. 3. Electronic properties of fcc potassium as a function of pressure. (a) Frequency of off-atom Bader maxima and average for fcc potassium at 50K (blue line) and 150K (green line). (b) Electron localization function (ELF) along [100] direction. The black arrows pointed out the center of the non-nuclear charge. (c)-(e) Electron localization function (ELF) along (001) slices of 50 K data at 9, 14, and 19 GPa, respectively. ELF values are shown in RGB scale from 0.0 (blue) to 0.7 (red). (f) AIMD snapshots of solid potassium (purple), sites of interstitial electron (green), and ELF = 0.7 isosurface (yellow). The N. e^- and N. Max are the average and maximum values of interstitial electrons, respectively.

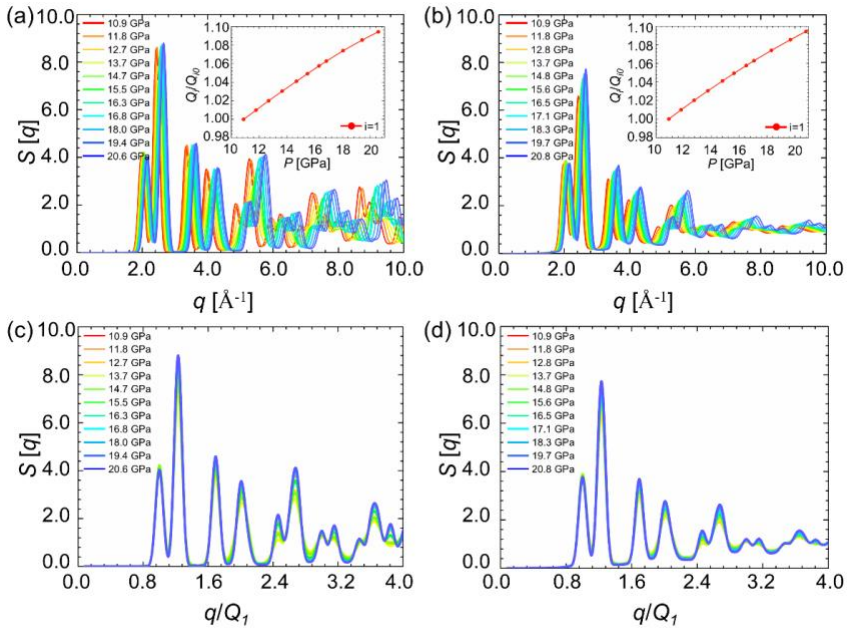

FIG. 4. Structural properties of solid potassium from MLMD simulations. Structure factor function at selected pressures for 50K (a) and 250K (b), respectively. The inset shows the relative location of the first peaks (Q_1/Q_{10}) as a function of pressure (where Q_1 is the location of the first peak in $S(q)$ at selected pressures while Q_{10} is the reference position of the first peak at 10.9 GPa). Normalized structure factor function by Q_1 at selected pressures for 50K (c) and 250K (d), respectively.

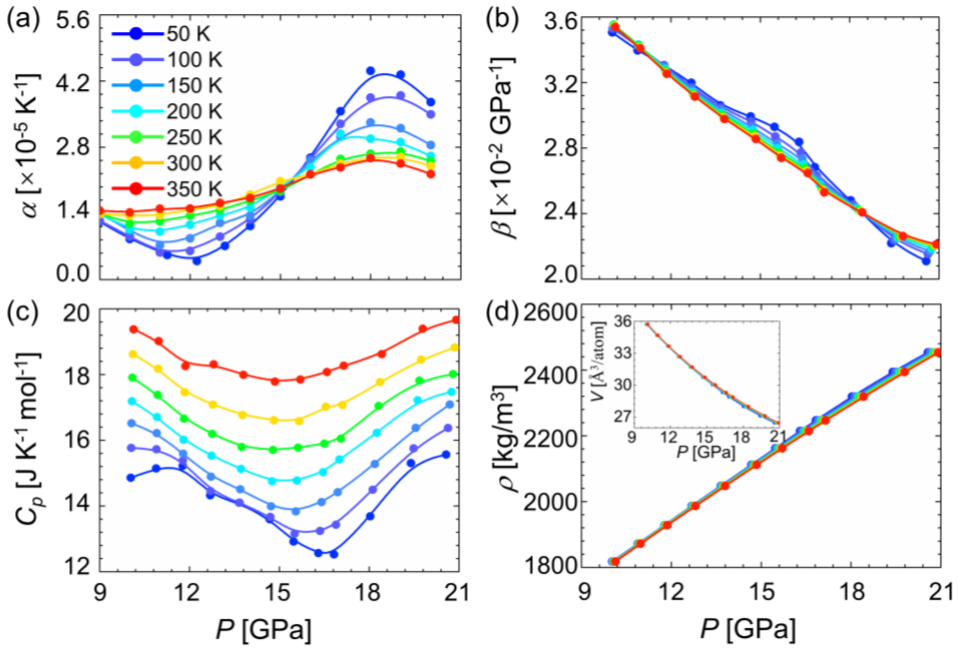

FIG. 5. Thermodynamic properties of solid potassium, shown as a function of pressure for selected temperatures. (a) Thermal expansivity α. (b) Compressibility β. (c) Heat capacity C_p. (d) Equation of state $\rho(P)$ (the insert shows the $V(P)$).

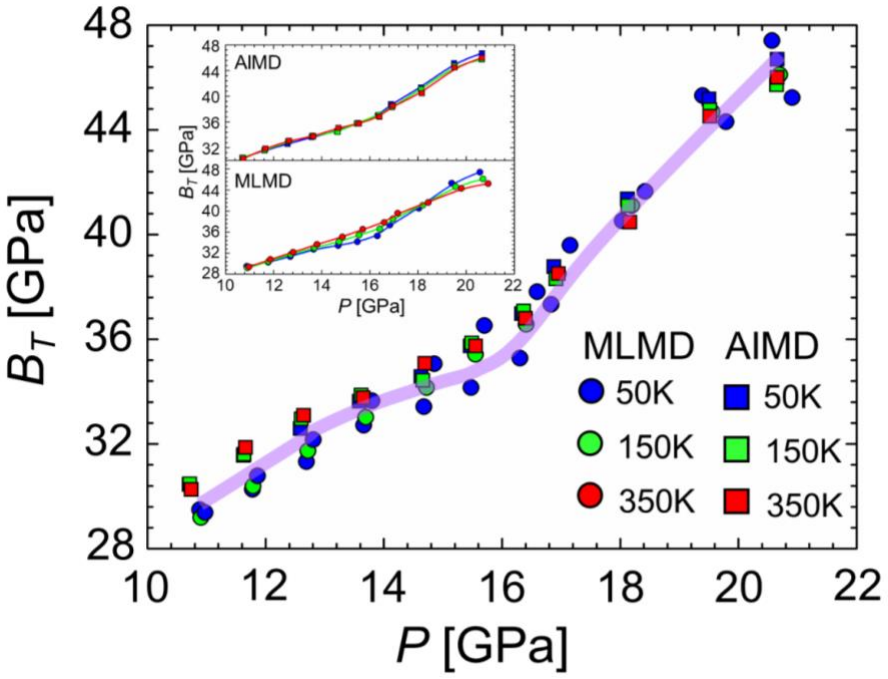

FIG. 6. Comparison of isothermal bulk modulus for MLMD and AIMD data at 50K, 150K, and 350K. The purple line is used to guide the eyes. The insert shows the temperature effect in MLIP and AIMD simulation data.

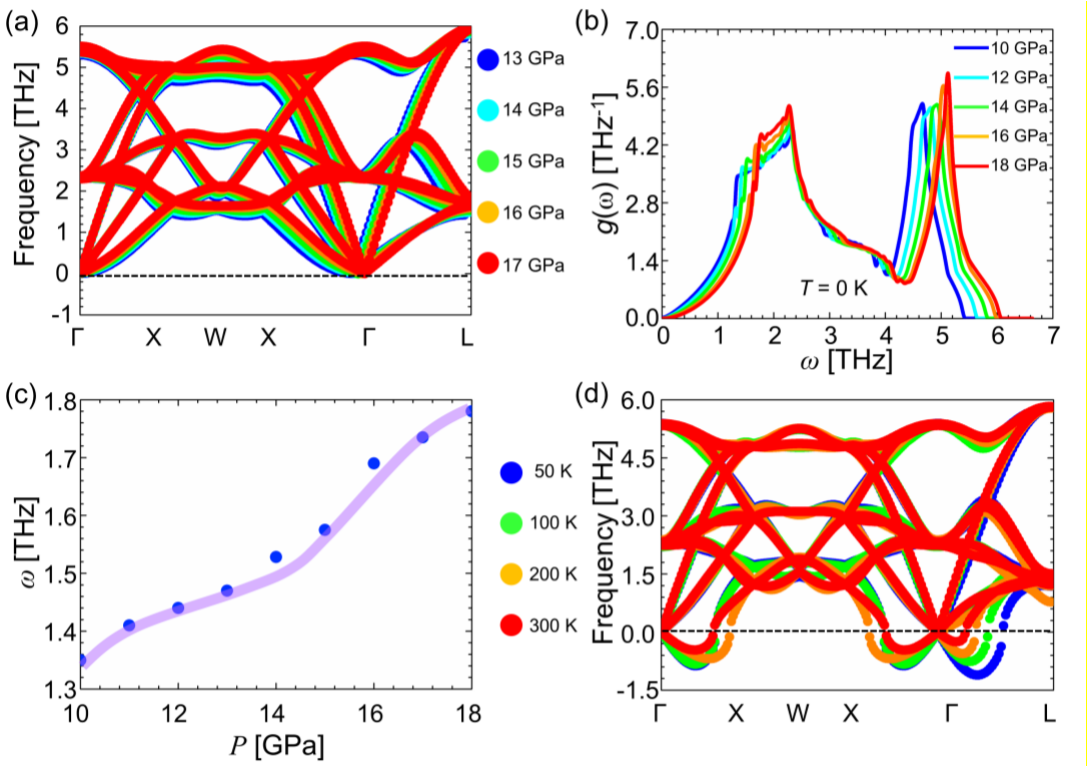

FIG. 7. Lattice vibration manner of fcc potassium across electride transition. (a) Phonon dispersion of fcc structure at selected pressures and 0 K. (b) Pressures effect on the vibrational density of states VDOS at 0 K. (c) The frequency of the first main peak (at ~ 1.5 THz) as a function of pressure. (e) Temperature effect on phonon dispersion at 14 GPa.

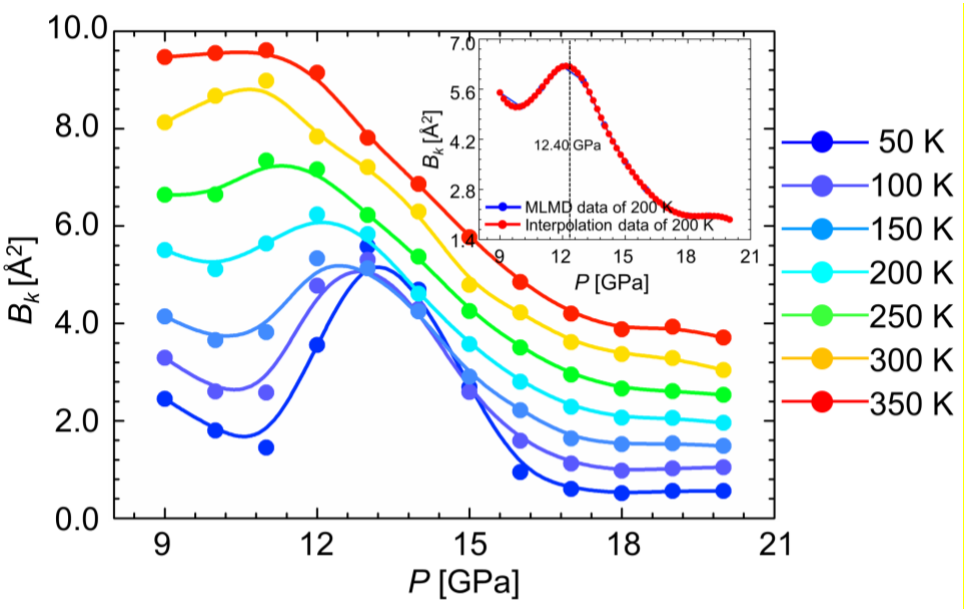

FIG. 8. Debye-Waller factor (B_k) of solid potassium from MLMD simulation at different temperatures. It characterizes the effect of lattice vibrations as a function of pressure. The inset is the data points of B_k upon compression at 200 K, whose cubic spline interpolation is used to determine the maximum point of B_k.

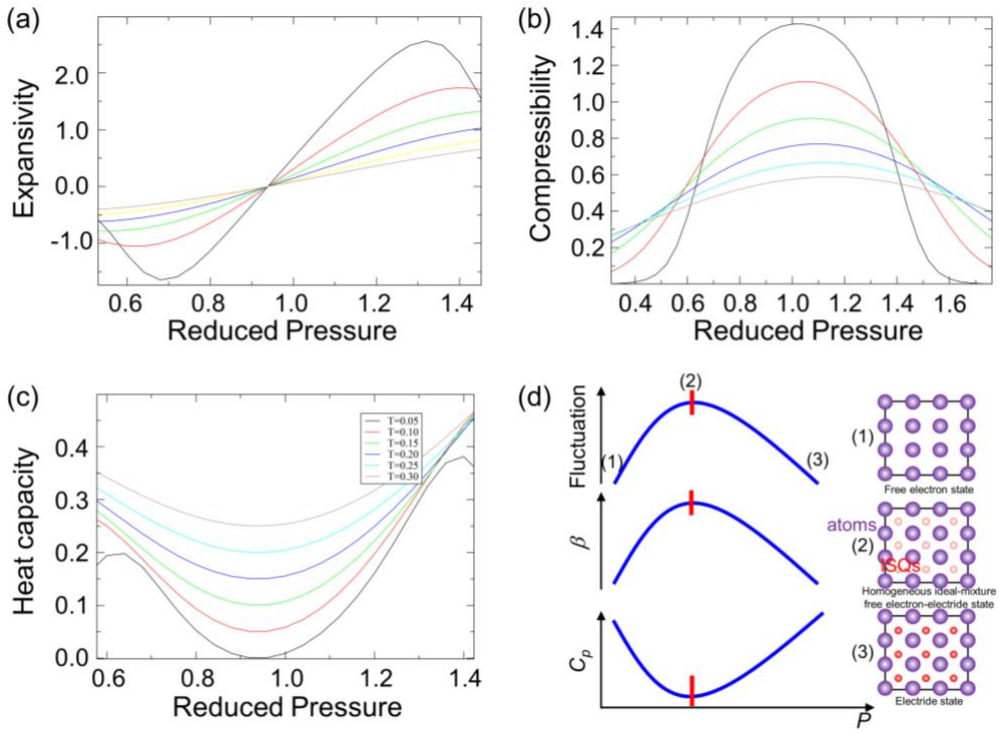

FIG. 9. Thermodynamic anomalies predicted by the Bragg-Williams-type model. Here, the parameters of the model are set as $U_0 = 1.0$, $V_0 = 1.0$, $J = -0.25$, and $S = 0.5$ in reduced units. Thermal expansivity (a), compressibility (b), and heat capacity (c) are calculated at different temperatures in reduced units. (d) A simplified picture of the correlation between thermal fluctuation induced by electride transition and anomalous thermodynamic responses.

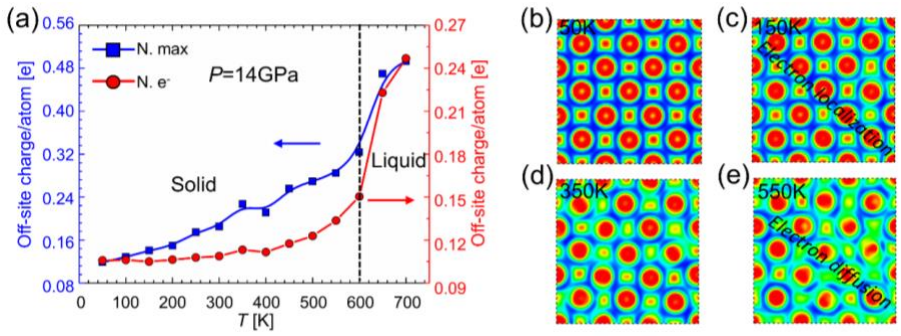

FIG. 10. Electronic properties of fcc potassium during heating. (a) The frequency of off-atom Bader maxima (blue line) and average (red line) as a function of temperatures at 14 GPa. (b)-(e) Electron localization function (ELF) along (001) slices in simulation snapshots at 14 GPa and (50, 150, 350, 550) K. ELF values are shown in RGB scale from 0.0 (blue) to 0.7 (red).